Histogram Analysis of IVIM MRI Parameters for Distinguishing Pseudo-progression and True Progression in High-Grade Gliomas

Mohammad Ghorbani (PhD)[1,2], Mohammad Ali Oghabian (PhD)[1,2*], Samira Raminfard (PhD)[2,3], Nahid Sadighi (MD)[3,4], Mostafa Farzin (MD)[5,6]

[1]Department of Medical Physics and Biomedical Engineering, School of Medicine, Tehran University of Medical Sciences, Tehran, Iran
[2]Neuroimaging and Analysis Group, Research Center for Molecular and Cellular Imaging, Advanced Medical Technologies and Equipment Institute, Tehran University of Medical Sciences, Tehran, Iran
[3]Medical Imaging Center of Imam Khomeini Hospital Complex (IKHC), Tehran University of Medical Sciences (TUMS), Tehran, Iran
[4]Advanced Diagnostic and Interventional Radiology Research Center (ADIR), Imam Khomeini Complex Hospital, Tehran University of Medical Sciences, Tehran, Iran
[5]Department of Radiation Oncology, Cancer Institute, IKHC, School of Medicine, Tehran University of Medical Sciences, Tehran, Iran
[6]Brain and Spinal Cord Injury Research Center, Neuroscience Institute, Tehran University of Medical Science, Tehran, Iran

*Corresponding author: Mohammad Ali Oghabian Department of Medical Physics and Biomedical Engineering, School of Medicine, Tehran University of Medical Sciences, Tehran, Iran
E-mail: oghabian@sina.tums.ac.ir

Received: 8 January 2025
Accepted: 10 March 2025

ABSTRACT

Background: Differentiating pseudoprogression (PsP) from true progression (TP) in high-grade gliomas (HGGs) is challenging, as conventional Magnetic Resonance Imaging (MRI) lacks sufficient specificity. Intravoxel incoherent motion (IVIM) MRI, may improve diagnostic performance by providing insights into tumor microstructure.

Objective: To evaluate the diagnostic performance of IVIM MRI derived parameters histogram in distinguishing PsP from TP in HGG patients.

Material and Methods: In a prospective study, 30 patients with WHO grade III or IV gliomas, previously treated with standard therapy, underwent IVIM MRI. Parametric maps (*D*, *D**, *f*, and Apparent Diffusion Coefficient (ADC)) were normalized to contralateral white matter, and histogram features were extracted from enhancing lesions. Univariate analysis identified significant features, and multivariate logistic regression assessed their combined diagnostic performance. The model's diagnostic performance was evaluated using receiver operating characteristic (ROC) curve analysis, with Area Under Curve (AUC), sensitivity, specificity, and accuracy.

Results: Histogram analysis revealed significant differences in most histogram features of the *D*-ratio, *D**-ratio, and ADC-ratio between PsP and TP groups. The 50th percentile of the *D*-ratio and the 99th percentile of the *D**-ratio were identified as independent predictors in the final model, with AUC values of 0.79 and 0.728, respectively. The final model achieved an AUC of 0.853, demonstrating high sensitivity (93.8%), specificity (64.3%), and overall accuracy (80%), outperforming individual parameters.

Conclusion: The 50th percentile of the *D*-ratio and the 99th percentile of the *D**-ratio demonstrated significant discrimination power between PsP and TP. Their combination further enhanced diagnostic accuracy, making them valuable metrics for clinical decision-making in HGG management.

Keywords

Diffusion Magnetic Resonance Imaging; Glioma; Brain Neoplasms; Intravoxel incoherent motion MRI; IVIM MRI; Pseudoprogression

Introduction

High-grade gliomas (HGG) are among the most aggressive brain tumors, characterized by rapid progression, extensive heterogeneity, and poor survival outcomes despite multimodal treatment approaches [1]. The current standard of care advocates for maximal or supramaximal surgery, followed by a combination of radiotherapy and

temozolomide chemotherapy [2]. Following chemoradiotherapy, a critical challenge in the management of HGG patients is differentiating between pseudo-progression (PsP) and true progression (TP). PsP is characterized by a temporary rise in contrast enhancement resulting from treatment-related inflammation and necrosis, mimicking tumor progression on standard MRI. In contrast, TP signifies actual tumor growth and requires prompt therapeutic intervention [3].

Traditional imaging techniques, such as contrast-enhanced T1-weighted MRI, provide limited information for distinguishing PsP from TP due to their reliance on the blood-brain barrier integrity, which can be disrupted in both conditions [4, 5]. The overlap in imaging characteristics of PsP and TP on conventional MRI can result in diagnostic uncertainty, potentially leading to mismanagement [6]. Advanced MRI techniques, including diffusion-weighted imaging (DWI), perfusion-weighted imaging (PWI), and magnetic resonance spectroscopy (MRS), have been proposed to address these limitations. Each method offers unique insights into tumor biology: DWI reflects cellularity, PWI measures vascular parameters, and MRS evaluates metabolic changes within the tumor microenvironment [7-9].

Diffusion MRI is a cornerstone in neuro-oncology, assessing the microstructural environment of brain tissues by tracking water molecule motion, known as Brownian motion. It provides insights into cellular density with apparent diffusion coefficient (ADC) measurements aiding the differentiation of different tissues. However, the mono-exponential model used in conventional diffusion MRI may oversimplify complex tissue structures. Intravoxel incoherent motion (IVIM) imaging, a branch of diffusion MRI, enhances tissue characterization by distinguishing between diffusion and perfusion effects [10]. It models DWI signal decay as a combination of true molecular diffusion and perfusion-related pseudo-diffusion, extracting parameters like the diffusion coefficient (D), perfusion fraction (f), and pseudo-diffusion coefficient (D^*). These metrics provide detailed insights into tissue microstructure, with D reflecting tissue's water molecule diffusion, f representing the fraction of the signal attributed to microcirculation, and D^* representing perfusion-related incoherent microcirculation [11, 12]. By isolating these components, IVIM offers a more comprehensive assessment of tumor heterogeneity compared to conventional diffusion MRI.

Emerging evidence suggests that IVIM parameters can capture distinct pathological differences in brain tumors by providing a nuanced characterization of tumor microenvironments. IVIM diffusion MRI has been extensively applied in glioma grading [13, 14], distinguishing primary brain tumors from metastases [15], and characterizing diverse brain tumors [16]. Importantly, IVIM diffusion MRI is particularly well-suited for differentiating PsP from TP in high-grade glioma patients because TP lesions often exhibit distinct differences in cellularity and vascularity compared to PsP lesions. IVIM parameters provide indirect yet detailed information about these characteristics by quantifying true diffusion (cellularity) and perfusion-related pseudo-diffusion (vascularity) [17, 18].

Despite these capabilities, the application of IVIM diffusion MRI in differentiating PsP from TP remains limited, as only a few studies have explored this technique in this context [19-21]. This highlights the need for further research to address this critical diagnostic challenge.

This study employs IVIM diffusion MRI to differentiate PsP from TP in HGG patients by analyzing first-order histogram features of IVIM-derived parameters between PsP and TP cases. Through the integration of IVIM diffusion MRI into clinical workflows, the objective is to identify robust IVIM parameters that can refine the accuracy of treatment assessment and decision-making in the management of HGG.

Material and Methods

This prospective and single-center study was conducted in accordance with the ethical standards of the Declaration of Helsinki and was approved by the Ethics Committee of Tehran University of Medical Sciences. Between December 2020 and March 2023, patients diagnosed with WHO grade III and IV high-grade gliomas, who had completed standard treatment (surgery, radiotherapy, and chemotherapy), were enrolled in our study. This study initially enrolled 41 patients. However, 11 participants were excluded due to failing to meet the inclusion criteria. Inclusion criteria mandated a pre-treatment histopathological diagnosis of high-grade glioma, completion of the standard treatment regimen, an IVIM diffusion MRI performed within 6 months of finalizing standard therapy, and the presence of an enhancing lesion on MRI images obtained within this time frame. Exclusion criteria encompassed inadequate image quality attributable to motion or susceptibility artifacts, absence of enhanced lesion, and patient nonadherence with follow-up MRI scans. Follow-up MRI examination repeated at 2- to 4-month intervals. A total of 30 patients (16 females, 14 males; mean age ±SD: 47±15.58 years) met the inclusion criteria and were enrolled in the study. Based on pathological confirmation in 5 patients and follow-up MRI findings in the remaining 25 patients, participants were classified into two groups: PsP (n=14) and TP (n=16). The overall study workflow, including patient selection, MRI data processing, statistical analysis, and model performance evaluation, is summarized in Figure 1.

MRI Acquisition: Brain imaging was performed on a 3T scanner (Discovery MR750W; GE Healthcare, Milwaukee, USA) and included both conventional and advanced MRI sequences. Conventional MRI consisted of pre- and post-contrast T1-weighted, T2-weighted, and fluid-attenuated inversion recovery (FLAIR) sequences, with detailed settings provided in Table 1. Post-contrast T1-weighted imaging followed the intravenous injection of 0.1 mmol/kg gadolinium-DOTA (DOTAREM; Guerbet, France). The IVIM diffusion MRI sequence was set up in accordance with

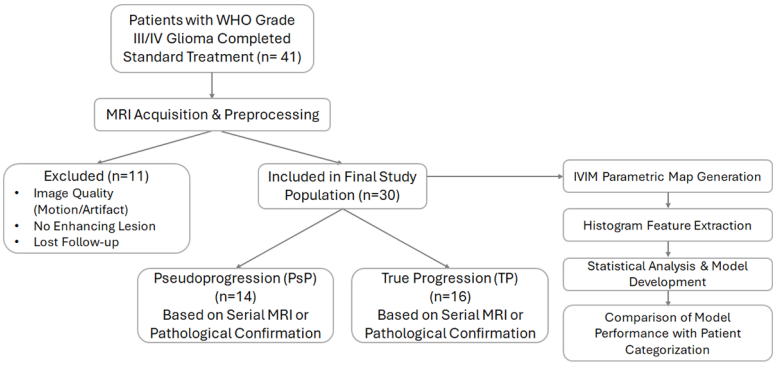

Figure 1: Study workflow, including patient selection, Magnetic Resonance Imaging (MRI) acquisition, data processing, and model evaluation. Patients with WHO grade III/IV gliomas who completed standard treatment were initially considered. A total of 11 patients were excluded due to poor image quality, absence of enhancing lesions, or loss of follow-up. The final study population consisted of 30 patients, categorized into pseudo-progression (PsP, n=14) and true progression (TP, n=16) based on follow-up MRI findings or pathological confirmation. The IVIM diffusion MRI data underwent preprocessing, parametric map generation, and histogram feature extraction. Statistical analysis was performed to develop a diagnostic model, whose performance was compared against patient categorization based on follow-up MRI and pathology findings.

the study by Hu et al. [22] and acquired before contrast injection, using 11 b-values (0, 20, 40, 60, 80, 100, 200, 400, 600, 800, and 1000 s/mm²) in three orthogonal directions. The number of signal averages for each b-value was adjusted to optimize signal to noise ratio (SNR), with 1 average for b-values between 0 and 200 s/mm², 2 for 400 s/mm², 3 for 600 s/mm², and 4 for 800 and 1000 s/mm².

IVIM Parametric Maps: Figure 2 shows IVIM parametric maps, generated using MITK Diffusion software (version 2.0.1) by fitting the IVIM data to Equation 1:

$$\frac{S_b}{S_0} = fe^{-(b\times D^*)} + (1-f)e^{-(b\times D)} \qquad [1]$$

Where S_b is MRI signal intensity at a given b-value, S_0 is the signal intensity at a b-value equal to 0, f is the perfusion fraction, representing the fraction of the signal attributed to microcirculation, D^* is pseudo-diffusion coefficient (or D_p), representing the perfusion-related incoherent microcirculation, and D is

Table 1: Magnetic Resonance Imaging (MRI) acquisition parameters for T2-weighted (T2-w), T1-weighted (T1-w), Fluid-Attenuated Inversion Recovery (FLAIR), and Intravoxel Incoherent Motion (IVIM) MRI sequences used in the study.

	TR/TE/TI (ms)	FOV (mm)	Slice thickness/gap (mm)	Matrix size	Flip angle°	#b-values
T2-w	5500/100/-	220×220	4.5/1	384×384	90	-
T1-w	600/10/-	220×220	4.5/1	352×224	90	-
FLAIR	9000/136/2468	220×220	4.5/1	320×224	90	-
IVIM MRI	3000/90/-	240×240	4.5/1	96×96	90	11

TR: Time of Repetition, TE: Time of Echo, TI: Time of Inversion, FOV: Field of View

#number of b-values

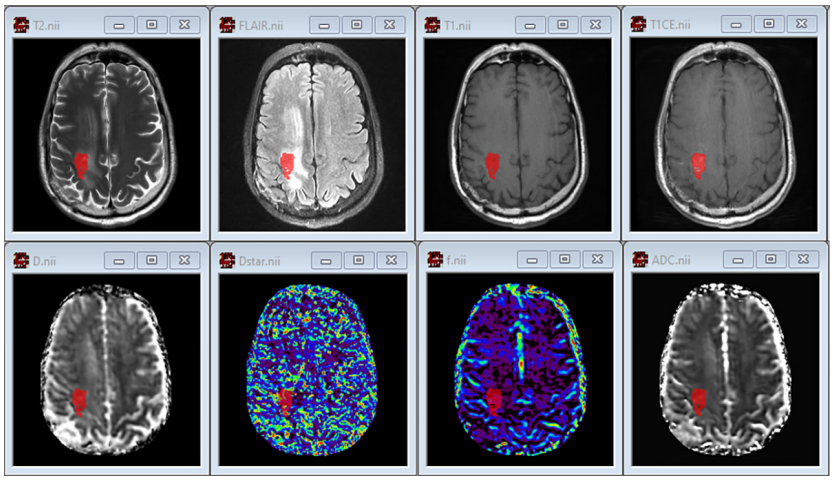

Figure 2: Anatomical images and parametric maps derived from Intravoxel Incoherent Motion Magnetic Resonance Imaging (IVIM MRI) for a representative case. The top row, arranged from left to right, displays anatomical images, including T2-weighted, Fluid-Attenuated Inversion Recovery (FLAIR), T1-weighted, contrast-enhanced T1-weighted (T1CE). The bottom row, also arranged from left to right, presents IVIM-diffusion maps: true diffusion coefficient (*D*), pseudo-diffusion coefficient (*D**), perfusion fraction (*f*), and apparent diffusion coefficient (ADC). The red overlay highlights the region of interest (ROI) within the enhancing lesion, which was used for quantitative histogram analysis.

true diffusion coefficient (or D_t), representing the tissue's water molecule diffusion [10].

This model employs a two-step fitting process to produce IVIM parametric maps. In the first step, data points at higher b-values (greater than approximately 200 s/mm²) are used to estimate the D and the f. These estimated values are then held constant while the model calculates the D^*.

The mono-exponential model was used to generate the ADC map using Equation 2:

$$S_b = S_0 e^{-(b \times ADC)} \quad [2]$$

Based on an exponential relationship between signal intensity and diffusion weighting (b-value), this model estimates the ADC of water molecules within tissues. To accomplish this, it was fitted to IVIM data acquired at two specific b-values: 0 s/mm² and 1000 s/mm².

Image registration: Anatomical images (FLAIR, T1-w, T1-w CE) and IVIM-diffusion parametric maps were meticulously registered to the T2-w images for each patient using ITK-SNAP 4.2.0. A rigid transformation model, including translation and rotation, was applied to preserve the shape and size of the images. Registration was performed in automatic mode, with anatomical images as the fixed reference and IVIM maps as the moving images. After registration, the aligned images were visually inspected to ensure proper anatomical correspondence, verifying that regions of interest were accurately matched.

IVIM parametric maps normalization: To calculate normalized IVIM parametric maps, a region of interest (ROI), sized 25 to 30 mm², was drawn in the normal-appearing white matter (NAWM) on an axial slice of the T2-weighted images in the hemisphere contralateral to the lesion for each case. Careful attention was given to avoid regions affected by susceptibility artifacts and brain ventricles. The NAWM ROI served as a reference for normalization, facilitating inter-patient comparisons by accounting for individual variations in baseline diffusion characteristics. Normalization was automatically performed using the freely available software package FireVoxel (build 456; https://FireVoxel.org). FireVoxel divided all pixel values of the registered IVIM parametric maps by the corresponding NAWM mean values.

Enhanced lesion segmentation: The subtraction tool in FireVoxel was used to segment the enhanced lesion. To improve visualization of the enhancing lesion, subtracted T1-weighted images were obtained by subtracting pre-contrast from post-contrast T1-weighted scans. Then a volume of interest (VOI) was drawn on the enhanced region of the lesion in subtracted images using the ROI drawing tool. Areas with necrosis, hemorrhage, or large blood vessels (visible on post-contrast T1-weighted or T2-weighted FLAIR images) were excluded from the VOI. The VOI was then transferred to the registered normalized IVIM parametric maps.

Histogram Features Calculation: Following the transfer of the VOI onto the registered normalized IVIM parametric maps, histogram features were calculated and extracted within VOI using the radiomics feature analysis tool within FireVoxel. Histogram features included minimum, maximum, mean, and various percentiles (1st, 5th, 10th, 25th, 50th [median], 75th, 90th, 95th, and 99th), reflecting the distribution of voxel intensities within the VOI.

Statistical Analysis: Statistical analysis was performed using IBM SPSS Statistics for Windows, version 27.0. The Shapiro-Wilk test was used to evaluate the normality of each IVIM MRI parameter's histogram features within the patient groups. Group comparisons were conducted using univariate analysis: independent samples t-tests for normally distributed features, and Mann-Whitney U tests for non-normally distributed features. Statistically significant differences (P-value<0.05) were identified for all histogram features of each IVIM parameter. To assess the discriminative ability of individual features within each IVIM parameter, receiver operating characteristic (ROC) curve analysis was performed. Features with

the highest area under the curve (AUC) were selected as those with the greatest discriminative potential for further analysis. Multivariate logistic regression analysis was subsequently employed to evaluate the combined diagnostic performance of these selected features in differentiating PsP from TP cases. The diagnostic performance of the final regression model was assessed using ROC analysis.

Results

A comparison of IVIM parameter ratios between PsP and TP cases, performed using univariate analysis, revealed significant differences across multiple histogram-derived features.

For the ADC-ratio, most features, excluding the maximum and 99th percentile, were elevated in the PsP group compared to the TP group. Significant differences were observed in the minimum (*P*-value=0.031), maximum (*P*-value=0.046), mean (*P*-value=0.014), and percentiles at the 1st (*P*-value=0.046), 5th (*P*-value=0.034), 10th (*P*-value=0.022), 25th (*P*-value=0.017), 50th (*P*-value=0.013), and 75th (*P*-value=0.028).

For the *D*-ratio, significant differences were found in the minimum value (*P*-value=0.011), mean value (*P*-value=0.008), and percentiles at the 1st (*P*-value=0.010), 5th (*P*-value=0.008), 10th (*P*-value=0.008), 25th (*P*-value=0.010), 50th (*P*-value=0.005), 75th (^{P}-value=0.011), and 90th (*P*-value=0.047). Most features were higher in the PsP group, while the maximum value and 99th percentile were elevated in the TP group.

For the *D**-ratio, significant differences were observed in the maximum value (*P*-value=0.014) and percentiles at the 75th (*P*-value=0.037), 90th (*P*-value=0.014), 95th (*P*-value=0.012), and 99th (*P*-value=0.010). All histogram features of the *D**-ratio were consistently higher in the TP group.

For the *f*-ratio, all histogram features were higher in the TP group compared to the PsP group, but only the maximum value demonstrated a borderline significant difference (*P*-value=0.0507).

These findings provide a foundation for subsequent multivariate analysis to evaluate the collective diagnostic efficacy of these histogram features and identify the most discriminative parameters for differentiating between PsP and TP cases. Based on the AUC metrics calculated for the significantly different histogram features, the following features were selected for multivariate analysis: the 50th percentile of the *D*-ratio (AUC=0.79, 95% CI: 0.612 to 0.968), the 99th percentile of the *D**-ratio (AUC=0.728, 95% CI: 0.532 to 0.923), the maximum value of the f-ratio (AUC=0.71, 95% CI: 0.524 to 0.896), and the mean value of the ADC-ratio (AUC=0.763, 95% CI: 0.576 to 0.950). Figure 3 illustrates the comparison of these selected histogram features of normalized IVIM parameters between the patient groups.

A logistic regression analysis using a forward selection procedure identified the 50th percentile of the *D*-ratio (*P*-value=0.025, SE=0.777) and the 99th percentile of the *D**-ratio (*P*-value=0.045, SE=0.293) as significant predictors for distinguishing PsP from TP cases. These parameters were retained in the final model. The ROC analysis of the final logistic regression model demonstrated superior predictive performance (AUC=0.853, 95% CI: 0.715 to 0.990) in distinguishing PsP from TP cases compared to the individual IVIM parameters, specifically the 50th percentile of the *D*-ratio (AUC=0.79, 95% CI: 0.612 to 0.968) and the 99th percentile of the *D**-ratio (AUC=0.728, 95% CI: 0.532 to 0.923). Figure 4 illustrates the ROC curves generated from this analysis.

Table 2 presents the performance metrics of the logistic regression model and its constituent IVIM parameters in differentiating PsP from TP.

Discussion

Magnetic resonance DWI measures the movement of water molecules within living tissues, reflecting the tissue microenvironment

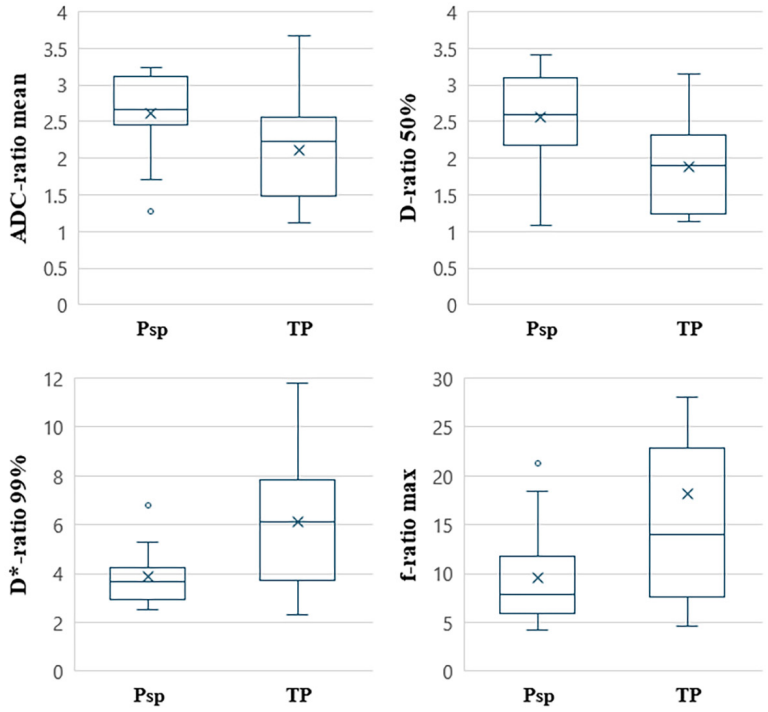

Figure 3: Comparison of selected histogram features of normalized Intravoxel Incoherent Motion Magnetic Resonance Imaging (IVIM MRI) parameters between pseudo-progression (PsP) and true progression (TP) groups. Box plots illustrate the distribution of the 50th percentile of the *D*-ratio, the 99th percentile of the *D**-ratio, the maximum value of the *f*-ratio, and the mean value of the Apparent Diffusion Coefficient (ADC)-ratio. The horizontal line and cross within each box represent median value and mean value, respectively.

and allowing for the assessment and quantification of cell density [23]. However, traditional DWI does not account for microperfusion within tissues. To address this limitation, Le Bihan et al. [24] introduced IVIM imaging, which simultaneously evaluates water molecule diffusion and microperfusion within capillaries, providing parameters, such as true diffusion coefficient (*D*), pseudo diffusion coefficient (*D**), and perfusion fraction (*f*). IVIM has been widely applied in grading and prognostication of brain gliomas [17, 25], but relatively few studies have explored its role in distinguishing between TP and PsP in high-grade gliomas following treatment.

In this study, we utilized histogram analysis of normalized IVIM parameters to account for tumor heterogeneity and assessed the diagnostic capability of IVIM in differentiating TP from PsP. Given the heterogeneous nature of tumors, assessing lesions using multiple quantitative parameters likely provides a more comprehensive characterization. In addition to extracting multiple diffusion-related parameters, we employed histogram analysis to better address the heterogeneity of HGGs. Previous studies have suggested that histogram analysis is a robust approach for evaluating heterogeneous lesions [26-28]. This integrated approach, utilizing both multiple parameters and histogram analysis, allowed us to capture a more complete picture of the tumor microenvironment.

Our findings revealed that while several

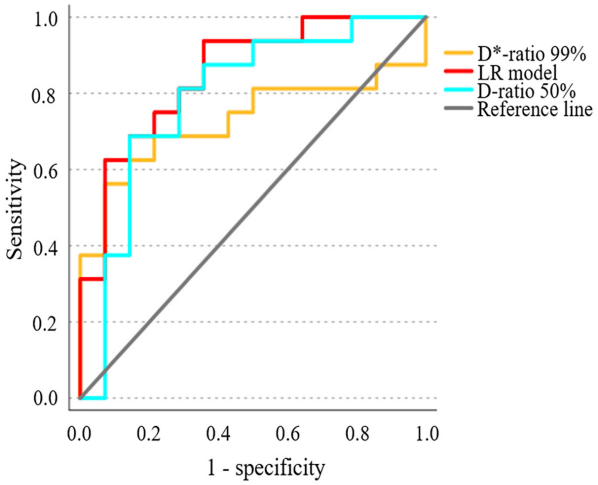

Figure 4: Receiver Operating Characteristic (ROC) curves for distinguishing pseudoprogression (PsP) from true progression (TP) groups based on the logistic regression (LR) model and individual normalized Intravoxel Incoherent Motion Magnetic Resonance Imaging (IVIM MRI) parameters. The red curve represents the ROC for the LR model, combining the 50th percentile of the *D*-ratio and the 99th percentile of the *D**-ratio. The cyan and yellow curves depict the ROC for individual parameters (50th percentile of the *D*-ratio and 99th percentile of the *D**-ratio, respectively). Patient classification was determined using follow-up Magnetic Resonance Imaging (MRI) findings (25 cases) and pathological sampling (5 cases) as reference standards. The LR model demonstrates superior diagnostic performance compared to single parameters.

histogram features derived from ADC and the IVIM parameters (*D*, *D**, and *f*) showed significant differences between TP and PsP patients in univariate analysis, the final multivariate model retained only the 50th percentile of the *D*-ratio and the 99th percentile of the *D**-ratio. Specifically, the 50th percentile of the *D*-ratio was lower in the TP group compared to the PsP group. This result aligns with the findings of Liao et al. who reported lower *D* values in TP compared to PsP, highlighting the potential of *D* in differentiating these conditions [29]. The reduced *D* values in TP group in our study likely result from increased tumor cellularity and reduced intercellular space, restricting water molecule diffusion. Conversely, PsP is characterized by treatment-induced changes, such as vasodilation, fibrinoid necrosis, and endothelial damage in normal cerebral vessels, resulting in higher water molecule diffusion within the enhanced portion of the lesion [30].

Additionally, the 99th percentile of the *D**-ratio was higher in the TP group compared to the PsP group, consistent with the findings of Kim et al. who observed increased *D** values in recurrent gliomas [19]. This may be attributed to the formation of immature blood vessels in TP. Tumor growth is often accompanied by angiogenesis, a process of new blood vessel formation. These newly formed vessels are typically structurally abnormal, exhibiting increased permeability and irregular shapes [31]. This leads to elevated perfusion-related parameters, such as *D**, reflecting the

Table 2: Diagnostic performance metrics of the logistic regression model and its constituent Intravoxel Incoherent Motion Magnetic Resonance Imaging (IVIM MRI) parameters for pseudoprogression (PsP) vs. true progression (TP) differentiation.

	Sensitivity (%)	Specificity (%)	Accuracy (%)	PPV (%)	NPV (%)	AUC
Predictive model	93.8	64.3	80	75	90	0.853
***D*-ratio 50%**	68.8	85.7	76.7	84.6	70.6	0.790
***D**-ratio 99%**	56.3	92.9	73.3	90	65	0.728

PPV: Positive Predictive Value, NPV: Negative Predictive Value, AUC: Area Under the Curve

increased microvascular perfusion in recurrent tumors.

Combining the *D*-ratio and the 99th percentile of the *D**-ratio improved diagnostic accuracy in distinguishing TP from PsP. This observation aligns with previous research indicating that combining multiple quantitative MRI parameters from a single advanced technique like IVIM MRI, with complementary information about tissue microstructure and micro-perfusion, can enhance diagnostic accuracy in differentiating tumor progression from treatment effects [32, 33].

In univariate analysis, the ADC-ratio demonstrated a significant difference between PsP and TP, with lower values in the TP group, consistent with findings in the literature [19, 29]. However, in multivariate analysis, ADC did not retain statistical significance and was excluded from the final model. This suggests that *D*, derived from the biexponential IVIM model, provides superior diagnostic accuracy for distinguishing TP from PsP. This is likely because *D*, as a pure molecular diffusion coefficient, is less susceptible to microcirculation-related biases compared to ADC, making it a more precise indicator of tumor cellularity. This finding aligns with studies indicating that biexponential models based on multiple b-values provide more reliable and accurate diffusion measurements than monoexponential models used for ADC calculation [34, 35]. This highlights the advantage of IVIM over conventional DWI in this specific clinical context.

The perfusion fraction (*f*) was another IVIM parameter excluded from the multivariate model. Although the maximum *f*-ratio value was higher in the TP group, its significance was borderline, and other histogram features of the *f*-ratio failed to reach statistical significance. While prior studies [19, 29] suggested the potential utility of *f* in differentiating PsP from TP, our findings were inconsistent. These discrepancies likely arise from several factors related to the inherent complexity and limitations of the IVIM model. Firstly, the accuracy of perfusion-related parameters like *f* is highly sensitive to the choice of fitting algorithm, optimization parameters, and b-value configuration, with no current consensus on the optimal b-value scheme for IVIM studies in brain tumors [34, 35]. Secondly, IVIM is known to be susceptible to noise, which can significantly affect *f* estimation. This is particularly relevant in postoperative imaging where susceptibility artifacts from surgical materials degrade the signal-to-noise ratio [36]. Air-tissue interfaces, such as those near the frontal sinus or skull base, further exacerbate noise-related inaccuracies in *f* estimation [37]. Finally, methodological variations in ROI delineation strategies may also contribute to the discrepancies in *f*-ratio findings. While, this study used whole-enhanced lesion ROIs, some prior studies employed hotspot ROI strategies, focusing on regions of maximum activity [19, 21, 29]. This difference in ROI selection could lead to a different sampling of tumor heterogeneity and therefore affect perfusion parameter estimates.

Our study has several limitations. The primary limitation is the lack of universal histological confirmation. While pathological sampling remains the gold standard, it is often not clinically feasible for monitoring treatment response, and even when available, biopsies may not fully capture HGG heterogeneity. Therefore, consistent with routine clinical practice, we relied on follow-up MRI and clinical data for most participants, with pathological confirmation available only for a subset [38]. The relatively small sample size also limits the generalizability of our findings, necessitating replication in a larger, ideally multi-center cohort. Finally, the echo-planar imaging (EPI) based DWI acquisition is susceptible to artifacts from magnetic field inhomogeneities, causing geometric distortions and signal loss, especially near air-tissue interfaces [39, 40]. These distortions can affect ROI placement and thus IVIM parameters, particularly the

noise-sensitive perfusion fraction. While careful ROI placement was employed to mitigate this, residual distortion remains a potential confounder. Future studies using distortion correction or alternative diffusion sequences (e.g., readout-segmented EPI) could further minimize these artifacts.

Conclusion

This study highlights the potential of IVIM MRI as a robust imaging tool for distinguishing True progression from pseudoprogression in high-grade gliomas. By employing histogram analysis of IVIM-derived parameters, we demonstrated that *D*-ratio and *D**-ratio are key metrics with significant diagnostic value. Furthermore, the combination of *D*-ratio and *D**-ratio improved diagnostic accuracy, underscoring the value of integrating multiple parameters to account for tumor heterogeneity.

Authors' Contribution

The study was conceptualized and designed by M. Ghorbani and MA. Oghabian. Imaging data acquisition was carried out by S. Raminfard and M. Farsi. Clinical evaluation, determination of patient status, and contributions to data analysis were conducted by N. Sadighi and M. Farzin. Data analysis and interpretation were primarily performed by M. Ghorbani, with guidance and supervision from MA. Oghabian. All authors participated in interpreting the findings, critically reviewed the manuscript, and contributed to its final version.

Ethical Approval

The Ethics Committee of Tehran University of Medical Sciences approved the protocol of the study (Ethic cod: IR.TUMS.MEDICINE.REC.1400.621).

Informed Consent

All patients were duly informed, and consent forms were obtained for the utilization of their data in the context of our research.

Funding

This work is supported by the Tehran University of Medical Science (grant number: 1400-3-373-54834).

Conflict of Interest

None

References

1. Omuro A, DeAngelis LM. Glioblastoma and other malignant gliomas: a clinical review. *JAMA.* 2013;**310**(17):1842-50. doi: 10.1001/jama.2013.280319. PubMed PMID: 24193082.
2. Stupp R, Mason WP, Van Den Bent MJ, Weller M, Fisher B, Taphoorn MJ, et al. Radiotherapy plus concomitant and adjuvant temozolomide for glioblastoma. *N Engl J Med.* 2005;**352**(10):987-96. doi: 10.1056/NEJMoa043330. PubMed PMID: 15758009.
3. Brandsma D, Stalpers L, Taal W, Sminia P, Van Den Bent MJ. Clinical features, mechanisms, and management of pseudoprogression in malignant gliomas. *Lancet Oncol.* 2008;**9**(5):453-61. doi: 10.1016/S1470-2045(08)70125-6. PubMed PMID: 18452856.
4. Kruser TJ, Mehta MP, Robins HI. Pseudoprogression after glioma therapy: a comprehensive review. *Expert Rev Neurother.* 2013;**13**(4):389-403. doi: 10.1586/ern.13.7. PubMed PMID: 23545054.
5. Ebrahimpour A, Khoobi M, Riyahi Alam N, Masoumbeigi M, Tirgar F, Ebrahimi T. Reliable differentiation of necrosis and active metabolically contours of glioblastoma multiforme using susceptibility-based imaging. *Heliyon.* 2024;**10**(7):e28355. doi: 10.1016/j.heliyon.2024.e28355. PubMed PMID: 38571593. PubMed PMCID: PMC10987993.
6. Wang S, Martinez-Lage M, Sakai Y, Chawla S, Kim SG, Alonso-Basanta M, et al. Differentiating Tumor Progression from Pseudoprogression in Patients with Glioblastomas Using Diffusion Tensor Imaging and Dynamic Susceptibility Contrast MRI. *AJNR Am J Neuroradiol.* 2016;**37**(1):28-36. doi: 10.3174/ajnr.A4474. PubMed PMID: 26450533. PubMed PMCID: PMC7960225.
7. Hyare H, Thust S, Rees J. Advanced MRI Techniques in the Monitoring of Treatment of Gliomas. *Curr Treat Options Neurol.* 2017;**19**(3):11. doi: 10.1007/s11940-017-0445-6. PubMed PMID: 28349351.
8. Yang Y, Yang Y, Wu X, Pan Y, Zhou D, Zhang H, et al. Adding DSC PWI and DWI to BT-RADS

can help identify postoperative recurrence in patients with high-grade gliomas. *J Neurooncol.* 2020;**146**(2):363-71. doi: 10.1007/s11060-019-03387-6. PubMed PMID: 31902040.

9. Young RJ, Gupta A, Shah AD, Graber JJ, Chan TA, Zhang Z, et al. MRI perfusion in determining pseudoprogression in patients with glioblastoma. *Clin Imaging.* 2013;**37**(1):41-9. doi: 10.1016/j.clinimag.2012.02.016. PubMed PMID: 23151413. PubMed PMCID: PMC4755513.
10. Le Bihan D. What can we see with IVIM MRI? *Neuroimage*. 2019;**187**:56-67. doi: 10.1016/j.neuroimage.2017.12.062. PubMed PMID: 29277647.
11. Iima M, Le Bihan D. Clinical Intravoxel Incoherent Motion and Diffusion MR Imaging: Past, Present, and Future. *Radiology.* 2016;**278**(1):13-32. doi: 10.1148/radiol.2015150244. PubMed PMID: 26690990.
12. Wang DJJ, Le Bihan D, Krishnamurthy R, Smith M, Ho ML. Noncontrast Pediatric Brain Perfusion: Arterial Spin Labeling and Intravoxel Incoherent Motion. *Magn Reson Imaging Clin N Am*. 2021;**29**(4):493-513. doi: 10.1016/j.mric.2021.06.002. PubMed PMID: 34717841.
13. Hino T, Togao O, Hiwatashi A, Yamashita K, Kikuchi K, Momosaka D, Honda H. Clinical efficacy of simplified intravoxel incoherent motion imaging using three b-values for differentiating high- and low-grade gliomas. *PLoS One.* 2018;**13**(12):e0209796. doi: 10.1371/journal.pone.0209796. PubMed PMID: 30589912. PubMed PMCID: PMC6307720.
14. Wang X, Chen XZ, Shi L, Dai JP. Glioma grading and IDH1 mutational status: assessment by intravoxel incoherent motion MRI. *Clin Radiol*. 2019;**74**(8):651.e7-14. doi: 10.1016/j.crad.2019.03.020. PubMed PMID: 31014573.
15. Su Y, Cheng R, Guo J, Zhang M, Wang J, Ji H, et al. Differentiation of glioma and solitary brain metastasis: a multi-parameter magnetic resonance imaging study using histogram analysis. *BMC Cancer*. 2024;**24**(1):805. doi: 10.1186/s12885-024-12571-5. PubMed PMID: 38969990. PubMed PMCID: PMC11225204.
16. Yamashita K, Hiwatashi A, Togao O, Kikuchi K, Kitamura Y, Mizoguchi M, et al. Diagnostic utility of intravoxel incoherent motion mr imaging in differentiating primary central nervous system lymphoma from glioblastoma multiforme. *J Magn Reson Imaging.* 2016;**44**(5):1256-61. doi: 10.1002/jmri.25261. PubMed PMID: 27093558.
17. Togao O, Hiwatashi A, Yamashita K, Kikuchi K, Momosaka D, Yoshimoto K, et al. Measurement of the perfusion fraction in brain tumors with intravoxel incoherent motion MR imaging: validation with histopathological vascular density in meningiomas. *Br J Radiol.* 2018;**91**(1085):20170912. doi: 10.1259/bjr.20170912. PubMed PMID: 29412000. PubMed PMCID: PMC6190789.
18. Kopřivová T, Keřkovský M, Jůza T, Vybíhal V, Rohan T, Kozubek M, Dostál M. Possibilities of Using Multi-b-value Diffusion Magnetic Resonance Imaging for Classification of Brain Lesions. *Acad Radiol*. 2024;**31**(1):261-72. doi: 10.1016/j.acra.2023.10.002. PubMed PMID: 37932166.
19. Kim HS, Suh CH, Kim N, Choi CG, Kim SJ. Histogram analysis of intravoxel incoherent motion for differentiating recurrent tumor from treatment effect in patients with glioblastoma: initial clinical experience. *AJNR Am J Neuroradiol.* 2014;**35**(3):490-7. doi: 10.3174/ajnr.A3719. PubMed PMID: 23969343. PubMed PMCID: PMC7964718.
20. Liu ZC, Yan LF, Hu YC, Sun YZ, Tian Q, Nan HY, et al. Combination of IVIM-DWI and 3D-ASL for differentiating true progression from pseudoprogression of Glioblastoma multiforme after concurrent chemoradiotherapy: study protocol of a prospective diagnostic trial. *BMC Med Imaging*. 2017;**17**(1):10. doi: 10.1186/s12880-017-0183-y. PubMed PMID: 28143434. PubMed PMCID: PMC5286785.
21. Tunlayadechanont P, Panyaping T, Chansakul T, Hirunpat P, Kampaengtip A. Intravoxel incoherent motion for differentiating residual/recurrent tumor from post-treatment change in patients with high-grade glioma. *Neuroradiol J.* 2023;**36**(6):657-64. doi: 10.1177/19714009231173108. PubMed PMID: 37105183. PubMed PMCID: PMC10649527.
22. Hu YC, Yan LF, Han Y, Duan SJ, Sun Q, Li GF, et al. Can the low and high b-value distribution influence the pseudodiffusion parameter derived from IVIM DWI in normal brain? *BMC Med Imaging.* 2020;**20**(1):14. doi: 10.1186/s12880-020-0419-0. PubMed PMID: 32041549. PubMed PMCID: PMC7011602.
23. Galbán CJ, Hoff BA, Chenevert TL, Ross BD. Diffusion MRI in early cancer therapeutic response assessment. *NMR Biomed.* 2017;**30**(3):e3458. doi: 10.1002/nbm.3458. PubMed PMID: 26773848. PubMed PMCID: PMC4947029.
24. Le Bihan D, Breton E, Lallemand D, Aubin ML, Vignaud J, Laval-Jeantet M. Separation of diffusion and perfusion in intravoxel incoherent motion MR imaging. *Radiology*. 1988;**168**(2):497-505. doi: 10.1148/radiology.168.2.3393671. PubMed PMID: 3393671.
25. Luo H, He L, Cheng W, Gao S. The diagnostic value of intravoxel incoherent motion imaging in

differentiating high-grade from low-grade gliomas: a systematic review and meta-analysis. *Br J Radiol*. 2021;**94**(1121):20201321. doi: 10.1259/bjr.20201321. PubMed PMID: 33876653. PubMed PMCID: PMC8506177.

26. Lu D, Li Y, Lu H, Pillai JJ. Histogram-based analysis of cerebral blood flow using arterial spin labeling MRI in de novo brain gliomas: relationship to histopathologic grade and molecular markers. *Neuroradiology.* 2021;**63**(5):751-60. doi: 10.1007/s00234-020-02625-3. PubMed PMID: 33392733.
27. Meyer HJ, Leifels L, Hamerla G, Höhn AK, Surov A. Histogram Analysis Parameters Derived from Conventional T1- and T2-Weighted Images Can Predict Different Histopathological Features Including Expression of Ki67, EGFR, VEGF, HIF-1α, and p53 and Cell Count in Head and Neck Squamous Cell Carcinoma. *Mol Imaging Biol.* 2019;**21**(4):740-6. doi: 10.1007/s11307-018-1283-y. PubMed PMID: 30284155.
28. Mao J, Deng D, Yang Z, Wang W, Cao M, Huang Y, Shen J. Pretreatment structural and arterial spin labeling MRI is predictive for p53 mutation in high-grade gliomas. *Br J Radiol*. 2020;**93**(1115):20200661. doi: 10.1259/bjr.20200661. PubMed PMID: 32877208. PubMed PMCID: PMC8519656.
29. Liao D, Liu YC, Liu JY, Wang D, Liu XF. Differentiating tumour progression from pseudoprogression in glioblastoma patients: a monoexponential, biexponential, and stretched-exponential model-based DWI study. *BMC Med Imaging.* 2023;**23**(1):119. doi: 10.1186/s12880-023-01082-7. PubMed PMID: 37697237. PubMed PMCID: PMC10494379.
30. Prager AJ, Martinez N, Beal K, Omuro A, Zhang Z, Young RJ. Diffusion and perfusion MRI to differentiate treatment-related changes including pseudoprogression from recurrent tumors in high-grade gliomas with histopathologic evidence. *AJNR Am J Neuroradiol*. 2015;**36**(5):877-85. doi: 10.3174/ajnr.A4218. PubMed PMID: 25593202. PubMed PMCID: PMC4731220.
31. McGahan BG, Neilsen BK, Kelly DL, McComb RD, Kazmi SA, White ML, et al. Assessment of vascularity in glioblastoma and its implications on patient outcomes. *J Neurooncol.* 2017;**132**(1):35-44. doi: 10.1007/s11060-016-2350-3. PubMed PMID: 28102487. PubMed PMCID: PMC5479489.
32. Aslan K, Gunbey HP, Tomak L, Incesu L. The diagnostic value of using combined MR diffusion tensor imaging parameters to differentiate between low- and high-grade meningioma. *Br J Radiol.* 2018;**91**(1088):20180088. doi: 10.1259/bjr.20180088. PubMed PMID: 29770735. PMCID: PMC6209476.
33. Chen X, Lin L, Wu J, Yang G, Zhong T, Du X, et al. Histogram analysis in predicting the grade and histological subtype of meningiomas based on diffusion kurtosis imaging. *Acta Radiol.* 2020;**61**(9):1228-39. doi: 10.1177/0284185119898656. PubMed PMID: 31986895.
34. Jalnefjord O, Andersson M, Montelius M, Starck G, Elf AK, Johanson V, et al. Comparison of methods for estimation of the intravoxel incoherent motion (IVIM) diffusion coefficient (D) and perfusion fraction (f). *MAGMA*. 2018;**31**(6):715-23. doi: 10.1007/s10334-018-0697-5. PubMed PMID: 30116979.
35. Paganelli C, Zampini MA, Morelli L, Buizza G, Fontana G, Anemoni L, et al. Optimizing b-values schemes for diffusion MRI of the brain with segmented Intravoxel Incoherent Motion (IVIM) model. *J Appl Clin Med Phys.* 2023;**24**(6):e13986. doi: 10.1002/acm2.13986. PubMed PMID: 37031365. PubMed PMCID: PMC10243330.
36. Bagheri MH, Ahmadloo N, Rezaian S. Artifacts in magnetic resonance imaging after surgical resection of brain tumors. *Magn Reson Imaging.* 2013;**31**(5):700-2. doi: 10.1016/j.mri.2012.11.001. PubMed PMID: 23333580.
37. Neufeld A, Assaf Y, Graif M, Hendler T, Navon G. Susceptibility-matched envelope for the correction of EPI artifacts. *Magn Reson Imaging.* 2005;**23**(9):947-51. doi: 10.1016/j.mri.2005.07.011. PubMed PMID: 16310110.
38. Wang L, Wei L, Wang J, Li N, Gao Y, Ma H, et al. Evaluation of perfusion MRI value for tumor progression assessment after glioma radiotherapy: A systematic review and meta-analysis. *Medicine (Baltimore)*. 2020;**99**(52):e23766. doi: 10.1097/MD.0000000000023766. PubMed PMID: 33350761. PubMed PMCID: PMC7769293.
39. Stäb D, Bollmann S, Langkammer C, Bredies K, Barth M. Accelerated mapping of magnetic susceptibility using 3D planes-on-a-paddlewheel (POP) EPI at ultra-high field strength. *NMR Biomed.* 2017;**30**(4):e3620. doi: 10.1002/nbm.3620. PubMed PMID: 27763692.
40. Farahani K, Sinha U, Sinha S, Chiu LC, Lufkin RB. Effect of field strength on susceptibility artifacts in magnetic resonance imaging. *Comput Med Imaging Graph*. 1990;**14**(6):409-13. doi: 10.1016/0895-6111(90)90040-i. PubMed PMID: 2272012.